**Wind and Structures**, *Vol. 24, No. 5 (2017) 447-464*
DOI: https:// doi.org/10.12989/was.2017.24.5.447 

# Flutter performance of central-slotted plate at large angles of attack

Haojun Tang[1,3], Yongle Li[*1], Xinzhong Chen[2], K.M. Shum[3] and Haili Liao[1]

[1]*Department of Bridge Engineering, Southwest Jiaotong University, Chengdu 610031, China*
[2]*National Wind Institute, Department of Civil, Environmental and Construction Engineering, Texas Tech University, Lubbock, Texas 79409-1023, USA*
[3]*CLP Power Wind/Wave Tunnel Facility, The Hong Kong University of Science and Technology, Hong Kong, China*

*(Received October 4, 2016, Revised April 30, 2017, Accepted May 1, 2017)*

**Abstract.** The flutter instability is one of the most important themes need to be carefully investigated in the design of long-span bridges. This study takes the central-slotted ideal thin flat plate as an object, and examines the characteristics of unsteady surface pressures of stationary and vibrating cross sections based on computational fluid dynamics (CFD) simulations. The flutter derivatives are extracted from the surface pressure distribution and the critical flutter wind speed of a long span suspension bridge is then calculated. The influences of angle of attack and the slot ratio on the flutter performance of central-slotted plate are investigated. The results show that the critical flutter wind speed reduces with increase in angle of attack. At lower angles of attack where the plate shows the characteristics of a streamlined cross-section, the existence of central slot can improve the critical flutter wind speed. On the other hand, at larger angles of attack, where the plate becomes a bluff body, the existence of central slot further reduces the flutter performance.

**Keywords:** central-slotted plate; aerodynamic interference; flutter derivatives; flutter performance; large angles of attack

## 1. Introduction

Design and construction of long-span bridges faces many challenges to ensure their performance against strong wind. The flutter instability is one of the most important themes need to be carefully investigated. For the flutter suppression of long-span bridges, optimizing the deck cross-sectional shape is considered to be one of most effective means to control the flow pattern and improve the bridge flutter performance.

The twin-box or multiple-box sections have attracted great attention as these sections have a great potential of showing improved flutter performance and have been adopted in a number of bridge designs, such as the Xihoumen Bridge (Zhang *et al*. 2013), the Stonecutter Bridge (Zhu and Xu 2014), and the Yi Sun-sin Bridge (Lee *et al*. 2014). Sato *et al*. (2000) showed that the critical flutter wind speed increases with the increase in slot width at the center of the girder. Sato *et al*. (2002) confirmed through a full aeroelastic model test that a slotted box girder with a slot ratio of

∗Corresponding author, Professor, E-mail: lele@swjtu.edu.cn


http://www.techno-press.org/?journal=was&subpage=8 ISSN: 1226-6116 (Print), 1598-6225 (Online)

0.3 was applicable for a super long-span bridge. The slot ratio is defined as the ratio of slot width to the deck width. Diana *et al*. (2006) carried aerodynamic studies of the proposed Messina Strait Bridge with a multiple-box section. Kwok *et al*. (2012) investigated the aerodynamic performance of twin-box bridge sections using section model wind tunnel test, and found that the vortex shedding frequency gradually increases with increasing slot width. Trein *et al*. (2015) studied the unsteady pressure characteristics of twin-box bridge deck, and showed that the results of single-box investigations could be extended to twin-box sections. Yang *et al*. (2015) studied the flutter performance of twin-box bridge decks through experimental investigation and investigated the best slot ratio for flutter stability. Yang *et al*. (2015) analyzed the effects of center slots on the aerodynamic performance of five representative girder cross sections with various slot widths. Miranda *et al*. (2015) investigated the capabilities and limitations of RANS and LES based CFD simulations in reproducing the flow field around a twin-box deck section.

While the aforementioned studies have greatly improved our understanding of the aerodynamic performance and the mechanism of the twin-box deck sections, the aerodynamic characteristics and flutter performance of this type of cross sections at large angles of attack have not yet been fully explored. Increasing number of long span bridges are now constructed in complicated mountainous canyon area where strong wind shows large angle of attack. The flutter performance at larger angles of attack becomes an increasing concern for the design and construction of these bridges, calling for further investigations on the aerodynamic characteristics of twin-box sections and sections with central slots.

In this paper, actual cross-section of bridge is simplified as an ideal thin flat plate to analyze the effects of central slot at large angles of attack on flutter performance of bridge. The aerodynamic characteristics of upstream and downstream plates are analyzed using CFD simulations. The flutter derivatives are then extracted from the dynamic surface pressures on the vibrating plate section, and the critical flutter wind speed is determined for a target bridge. The effects of slot ratio and angle of attack are discussed.

## 2. Aerodynamic characteristics of central-slotted plate

### *2.1 CFD model*

The computational domain and boundary conditions are shown in Fig. 1. The computational conditions are given as follows: the ratio of plate width $B$ to thickness $H$ is 200, where $B$ is 0.7 m. The computational domain is assumed to be $24B$ in the mean-flow direction and $12B$ in the cross-flow direction. The distance of the plate center to the velocity inlet boundary is $6B$. The wind velocity at the inlet is uniform with a turbulence intensity of 0.5% and a turbulent viscosity ratio of 2.0 according to Huang *et al*. (2009). Different slot ratios are considered by keeping the global side ratio $B/H$ unchanged while increasing the central slot width $D$. The slot ratio $\varphi$ is defined as $D/B$. Meanwhile, the angles of attack ranging from 0°-10° are selected according to the measurement wind data at a bridge site located in mountainous canyon area.

Both calculations with stationary and vibrating plate sections are carried out to investigate the static (mean) surface pressure distribution and the characteristics of motion-induced unsteady surface pressure distribution. The computational mesh is shown in Fig. 2. In order to improve the calculation accuracy, the computational domain is divided into three regions, named as rigid mesh zone, dynamic mesh zone, and fixed mesh zone, respectively. The rigid mesh zone moves along

with the plate to ensure the quality of the mesh near the plate. The rigid mesh zone and the fixed mesh zone are discretized by a quadrilateral structured gird, and the dynamic mesh zone is discretized by a triangular unstructured gird. The element size progressively increased from the side of plate to the computational boundary. The mesh numbers for plate with different slot ratios are listed in Table 1. The height of the first layer of cells is $10^{-5}$ to ensure that the mean value of $y^+$ is less than 1 in both stationary and vibrating cases.

RANS simulations are performed by using the $k$-$\omega$ SST model. Such model is known to provide more accurate results, if compared to standard $k$-$\omega$ and $k$-$\varepsilon$ models, in external aerodynamic cases which involve boundary layer separation (Miranda *et al*. 2015). The dimensionless time-step has been set equal to $10^{-3}$. The discretized problem has been numerically solved by adopting a SIMPLE pressure-velocity coupling algorithm.

Table 1 Mesh numbers for different slot ratios

| Slot ratio $\varphi$ | 0% | 5% | 10% | 15% | 20% | 30% |
|---|---|---|---|---|---|---|
| Cells of rigid zone | 62,000 | 76,954 | 67,226 | 63,592 | 62,930 | 61,160 |
| Cells of dynamic zone | 79,558 | 120,594 | 106,712 | 106,774 | 111,670 | 147,874 |
| Cells of fixed zone | 28,000 | 28,000 | 28,000 | 28,000 | 28,000 | 28,000 |
| Total number | 169,558 | 225,548 | 201,938 | 198,366 | 202,600 | 237,034 |

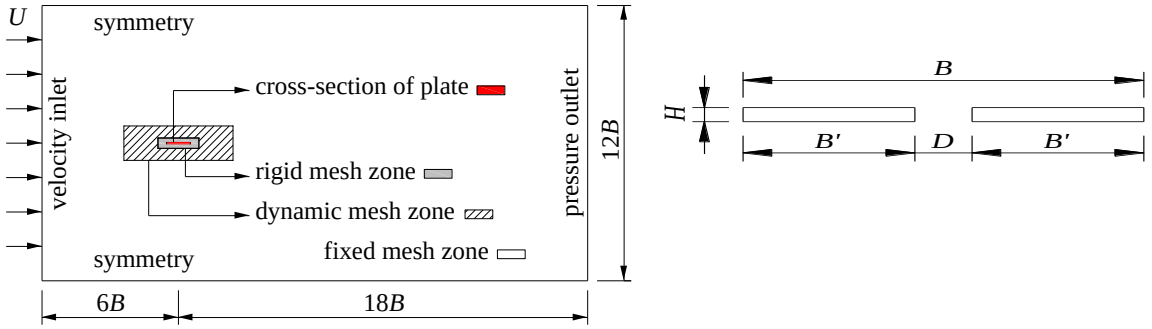


(a) Computational domain (b) Model section

Fig. 1 Computational domain and model section

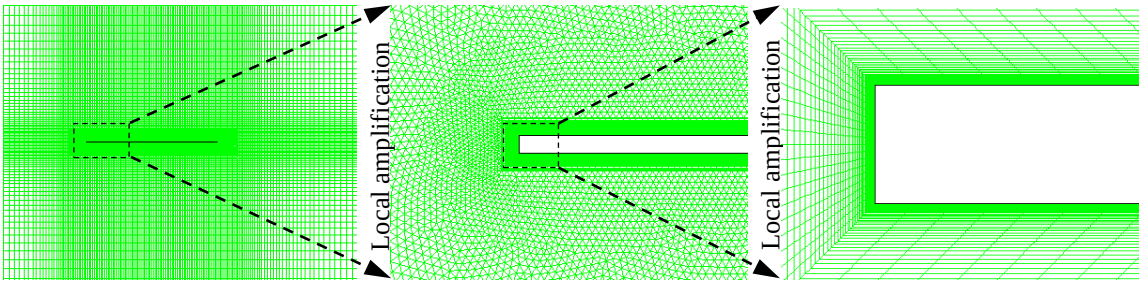


Fig. 2 Local computational mesh employed in numerical analysis

A second order scheme is selected for pressure, and a second order upwind scheme is selected for momentum, turbulent kinetic energy, and specific dissipation rate. The CFD software FLUENT is used in the simulation.

### *2.2 Aerodynamic interference of static cross sections*

The characteristics of surface pressures of the stationary central-slotted plate are firstly analyzed. From the distributed pressures, the lift and moment coefficients for upstream and downstream plates and for the overall slotted plate are calculated to understand the aerodynamic interference. For the plate without slot, the lift and moment coefficients are defined as Eqs. (1) and (2), respectively.

$$C_L(\alpha) = -L(\alpha)/(\tfrac{1}{2}\rho U^2 B) \tag{1}$$

$$C_M(\alpha) = M(\alpha)/(\tfrac{1}{2}\rho U^2 B^2) \tag{2}$$

where $L(\alpha)$ and $M(\alpha)$ are the lift force (downward) and pitching moment (nose-up), respectively; $\alpha$ is the angle of attack; $B$ is the width of plate; $\rho$ is the air density; and $U$ is the mean wind velocity and set to 14 m/s. For the central-slotted plate, $B$ is replaced with $B'$ for the single upstream or downstream plate and $2B'$ for the overall cross-section.

For plates with different slot ratios at different angles of attack, Fig. 3 shows the average lift and moment coefficients, $\bar{C}_L$ and $\bar{C}_M$. Fig. 4 shows the root mean square of lift coefficient, $C_L'$.

For the plate without slot, with the increase in angle of attack, the value of $\bar{C}_L$ increases and is relatively stable when the angle is larger than 6°, and the value of $\bar{C}_M$ increases but then decreases, showing a good agreement with the results reported by Amandolese *et al*. (2013). To eliminate the effects of mesh number on the results, the total mesh number is changed to 110,060, 138,244, and 244,632, and the results remain unchanged, as shown in Fig. 5.

For the overall slotted plates with different slot ratios, the values of $\bar{C}_L$ and $\bar{C}_M$ almost keep the same at lower angles of attack, but change obviously at larger angles of attack due to the aerodynamic interference between the two plates in tandem arrangement.

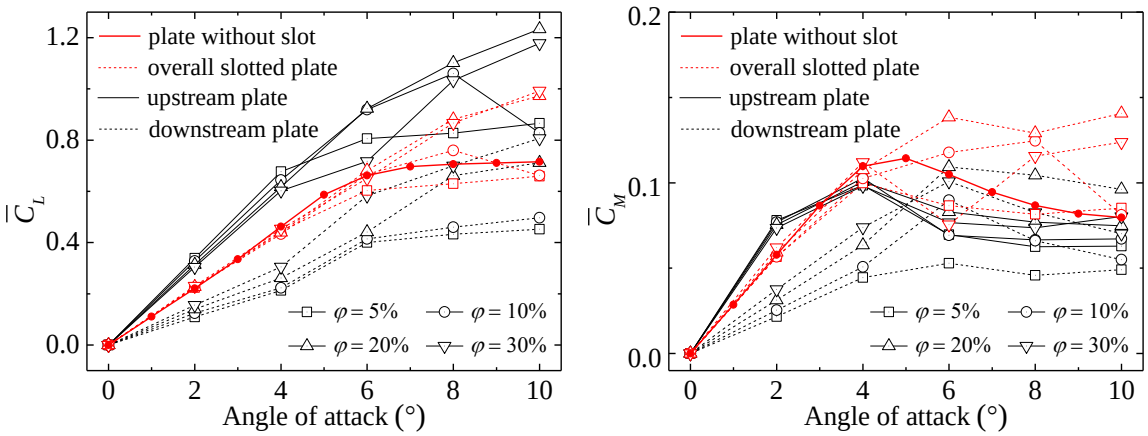


(a) Lift coefficients (b) Moment coefficients

Fig. 3 The average aerodynamic coefficients versus angle of attack

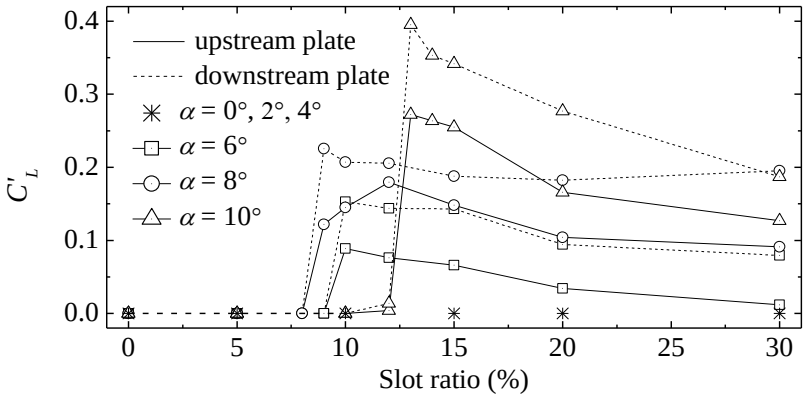


Fig. 4 The RMS lift coefficient versus slot ratio

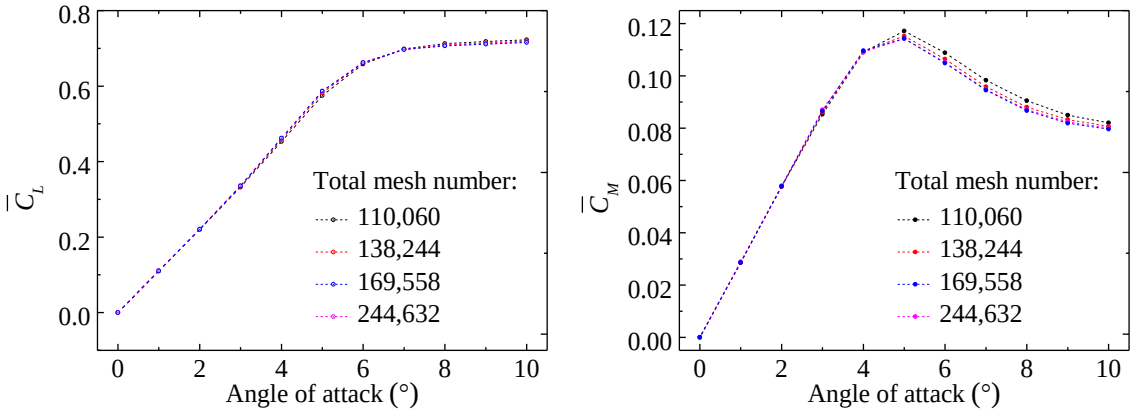


(a) Lift coefficients (b) Moment coefficients

Fig. 5 The average aerodynamic coefficients of the plate without slot

When the angle of attack is small, including 0°, 2° and 4°, the values of $\bar{C}_L$ of the upstream plate are larger than those of the plate without slot, but it is the opposite for the downstream plate. The values of $\bar{C}_M$ of the upstream plate are also larger than those of the downstream plate. Fig. 6 shows the streamline diagrams of mean velocity vector of fixed central-slotted plate with 0°, 2° and 4° angles of attack. The downstream plate has weak effects on the aerodynamic characteristics of the upstream plate, which, however, has obvious effects on the downstream plate. For the upstream plate, the size of the stable vortex formed on the leading edge is almost unchanged, so its average lift coefficient increases due to the decrease in width. Compared with the upstream plate, the vortex formed on the upper surface of the downstream plate is small, so its average lift and moment coefficients are also small. The average lift and moment coefficients for both plates are gradually close to the values of single plate with the increase in slot ratio.

When the angle of attack is large, including 6°, 8° and 10°, the variations of $\bar{C}_L$ and $\bar{C}_M$ become ruleless for both upstream and downstream plates. The values of $C_L'$ increase suddenly at certain slot ratios and then gradually decrease with the further increase in slot ratio. Fig. 6 also shows the streamline diagrams of mean velocity vector of fixed central-slotted plate with 6° and 8°

angles of attack respectively. The effects of central slot on the aerodynamic characteristics of plate are related to the slot ratio. At smaller slot ratios, a small stable vortex can exist between two big vortices formed above the upstream and downstream plates, so the values of $C_L'$ for both plates are still equal to zero. With the increase in slot ratio, the length of the small vortex is stretched. When the slot ratio increases to a critical value, the small vortex cannot stablely exist and the vortex shedding is excited, so time series of lift coefficient of both plates are fluctuant. As no vortex shedding phenomenon is observed for single independent upstream or downstream plate at the same angle of attack, the vortex shedding is indeed caused by the existence of central slot.

### *2.3 Motion-induced unsteady pressure distribution*

The unsteady pressure characteristics along the central-slotted plate are then analyzed. To derive the motion-induced pressures, single degree-of-freedom (SDOF) vibration in heaving and torsion is imposed respectively. The amplitude of single peak is set as $h_0$=0.025$B$ for heaving vibration, and $\alpha_0$=3° for torsional vibration. The plate center is set as the torsional center. The vibration frequency, $f$, is 2 Hz for both SDOF heaving and torsional vibrations.

The unsteady pressure components are expressed by the magnitude and phase difference. The magnitude, $\tilde{C}_p$, is the amplitude of the unsteady pressure fluctuation and normalized by the dynamic pressure of the flow, $0.5\rho U^2$. The phase difference, $\psi$, is defined as the phase lag of negative peak-pressure from the maximum relative angle of attack, defined by the maximum displacement (nose-up) for torsional vibration and the neutral position (downward) for heaving vibration. The information is discretized according to the non-dimensionalized (normalized by 0.5$B$) $x$ widthwise coordinate. This parameter is defined as $x^*$ and ranges from -1 to 1, where -1 and 1 are the leading edge and the trailing edge of the plate respectively and 0 is the center.

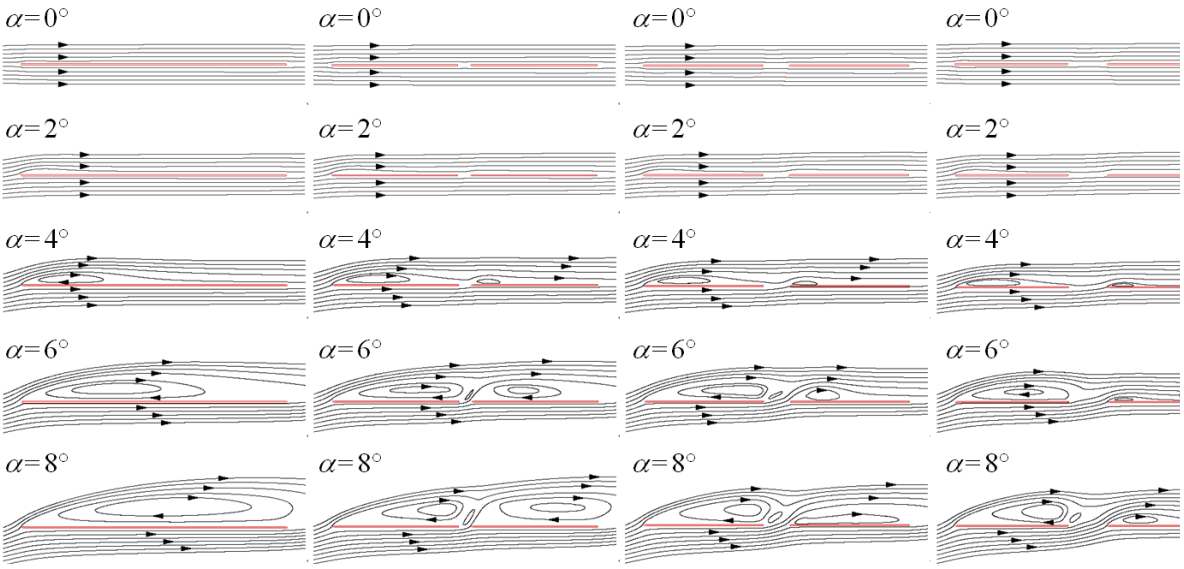


Fig. 6 Streamline diagrams of mean velocity vector

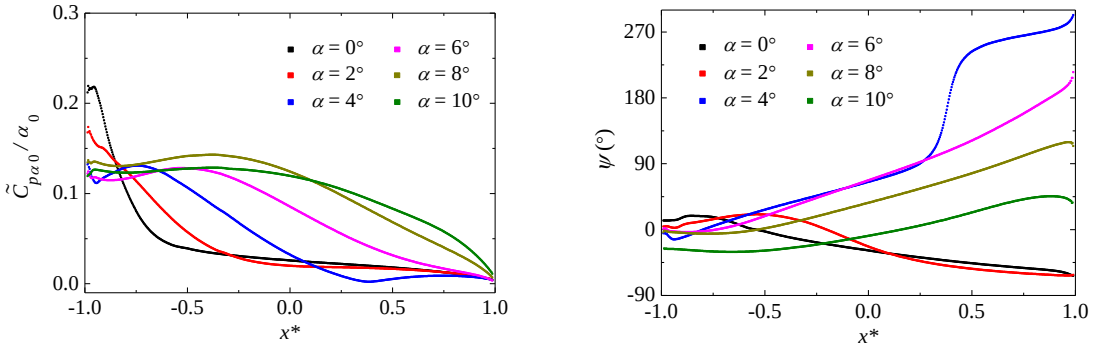


(a) Magnitude distributions (b) Phase difference distributions

Fig. 7 Unsteady pressure characteristics of plate without slot with torsional 1DOF

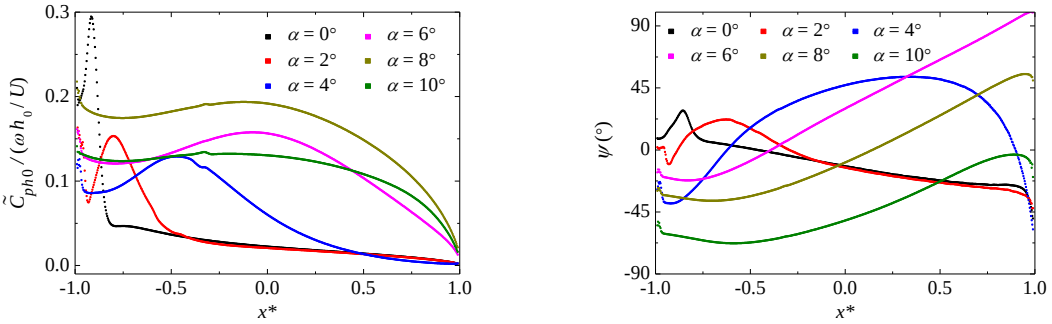


(a) Magnitude distributions (b) Phase difference distributions

Fig. 8 Unsteady pressure characteristics of plate without slot with heaving 1DOF

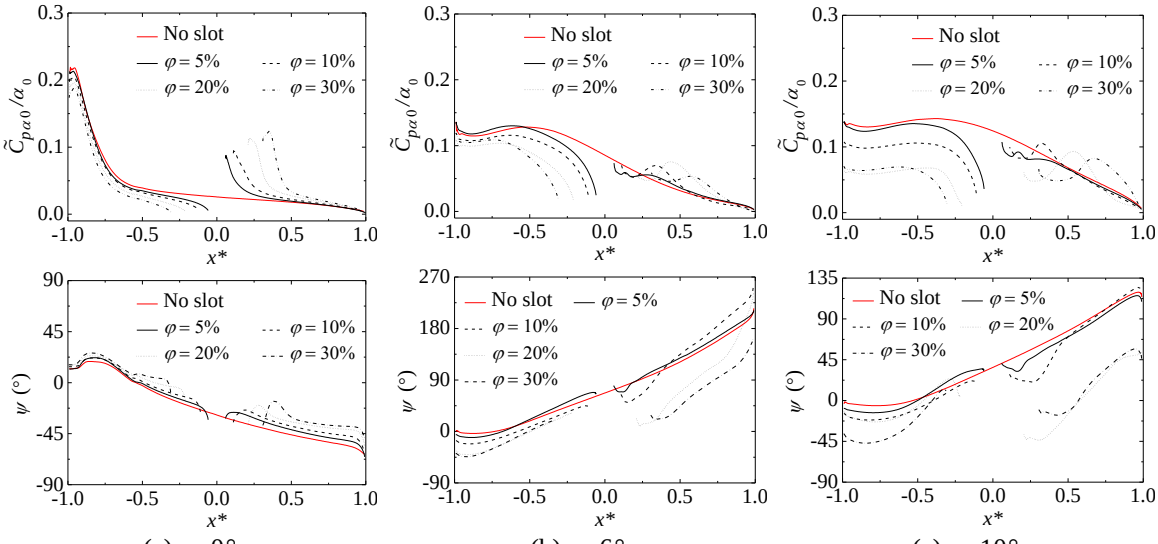


(a) $\alpha$=0° (b) $\alpha$=6° (c) $\alpha$=10°

Fig. 9 Unsteady pressure characteristics of central-slotted plate with torsional 1DOF

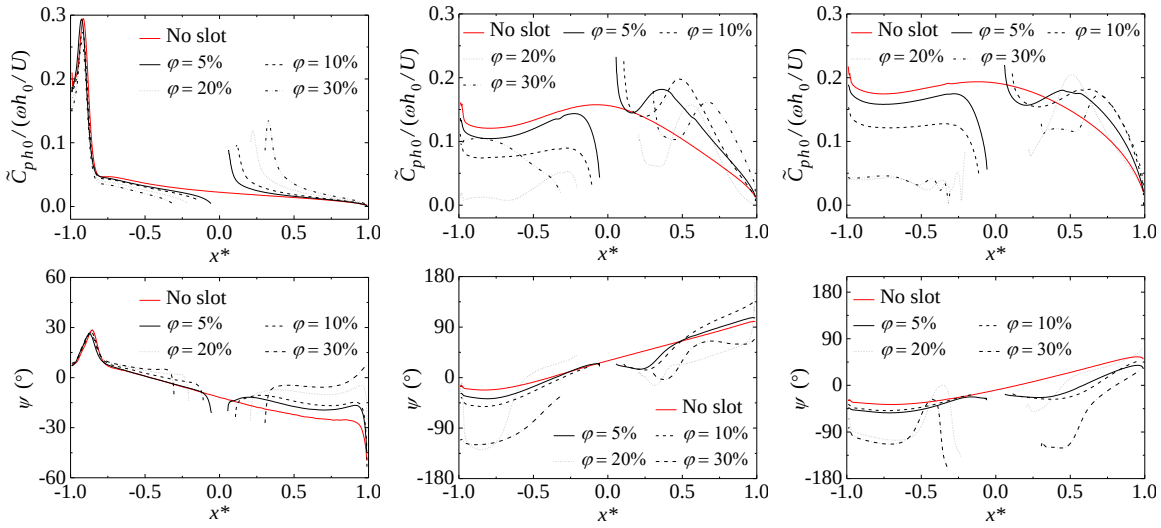


(a) $\alpha$=0° (b) $\alpha$=6° (c) $\alpha$=10°

Fig. 10 Unsteady pressure characteristics of central-slotted plate with heaving 1DOF

The reduced wind velocity, defined by $U/(f \cdot B)$, ranges from 2 to 10, in steps of 2. Larger reduced wind velocities or smaller steps are considered for partial cases. The change in reduced velocity is achieved by changing the mean wind speed, $U$. For the plate without slot, the distributions of the magnitude for unit relative angle of attack, $\tilde{C}_{p\alpha 0}(x^*)/\alpha_0$ for torsional vibration and $\tilde{C}_{ph0}(x^*)/(\frac{\omega h_0}{U})$ for heaving vibration, and the phase difference at a reduced wind velocity $U/(f \cdot B)$=10 are shown in Fig. 7 with torsional 1DOF and Fig. 8 with heaving 1DOF respectively. With the same relative angle of attack, the unsteady pressure distributions caused by torsion and heaving can have an easy comparison.

The magnitude and phase difference are sensitive to variation in angle of attack, and the two parameters have similarities in their respective distribution and change laws between the torsional and heaving vibrations. With the increase in angle of attack, the peak of the magnitude curve at the leading edge moves to the plate center and becomes gradual, and the increasing interval of phase difference from negative peak at the upwind side to positive peak becomes broader, which implies the size of the vortex in front of the plate and its movement distance along the plate gradually increase. The effects of the increasing angle of attack on the unsteady pressure characteristics are similar as those of the decreasing $B/D$ observed by Matsumoto (1996), who investigated the unsteady pressure characteristics of rectangular cylinders with side ratios varying from $B/D$=5 to $B/D$=20. Therefore, the streamlined plate presents the characteristics of bluff body at larger angles of attack during the vibration.

For the central-slotted plates with different slot ratios, the distributions of the magnitude for unit relative angle of attack and the phase difference at the same reduced wind velocity $U/(f \cdot B)$=10 are shown in Figs. 9 and 10 respectively. The central slot has the same effects on the aerodynamic characteristics of the vibration plate, compared with the stationary plate. At lower angles of attack, the central slot has little effects on the magnitude and phase difference distributions of the

upstream plate due to the weak aerodynamic interference caused by the downstream plate. With the increase in slot ratio, the unsteady pressure characteristics of the downstream plate are gradually close to those of the upstream plate. At larger angles of attack where the plate becomes a bluff body, the vortex shedding can also be caused by the central slot with large width during the vibration. Thus, the larger the slot ratio is, the bigger the unsteady pressure characteristics of the two plates change.

### *2.4 Flutter derivatives*

The Scanlan's linearized theory of flutter derivatives is widely used to estimate the critical flutter wind speed. Flutter derivatives can be extracted from wind tunnel test or numerical simulation by free or forced vibration. Through the measurement of the magnitude and phase difference distributions, eight flutter derivatives can be obtained from the following equations

For torsional motion

$$H_2^* = \left(\frac{U}{fB}\right)^2 \frac{1}{8\pi^2\alpha_0}\int_{-1}^{1} \tilde{C}_{p\alpha 0}(x^*)\sin\left(\psi_\alpha(x^*)\right)dx^* \tag{3}$$

$$H_3^* = -\left(\frac{U}{fB}\right)^2 \frac{1}{8\pi^2\alpha_0}\int_{-1}^{1} \tilde{C}_{p\alpha 0}(x^*)\cos\left(\psi_\alpha(x^*)\right)dx^* \tag{4}$$

$$A_2^* = \left(\frac{U}{fB}\right)^2 \frac{1}{8\pi^2\alpha_0}\int_{-1}^{1} x^*\tilde{C}_{p\alpha 0}(x^*)\sin\left(\psi_\alpha(x^*)\right)dx^* \tag{5}$$

$$A_3^* = -\left(\frac{U}{fB}\right)^2 \frac{1}{8\pi^2\alpha_0}\int_{-1}^{1} x^*\tilde{C}_{p\alpha 0}(x^*)\cos\left(\psi_\alpha(x^*)\right)dx^* \tag{6}$$

For heaving motion

$$H_1^* = -\left(\frac{U}{fB}\right)^2 \frac{1}{8\pi^2(h_0/B)}\int_{-1}^{1} C_{ph0}(x^*)\cos\left(\psi_h(x^*)\right)dx^* \tag{7}$$

$$H_4^* = -\left(\frac{U}{fB}\right)^2 \frac{1}{8\pi^2(h_0/B)}\int_{-1}^{1} C_{ph0}(x^*)\sin\left(\psi_h(x^*)\right)dx^* \tag{8}$$

$$A_1^* = -\left(\frac{U}{fB}\right)^2 \frac{1}{8\pi^2(h_0/B)}\int_{-1}^{1} x^*C_{ph0}(x^*)\cos\left(\psi_h(x^*)\right)dx^* \tag{9}$$

$$A_4^* = -\left(\frac{U}{fB}\right)^2 \frac{1}{8\pi^2(h_0/B)}\int_{-1}^{1} x^*C_{ph0}(x^*)\sin\left(\psi_h(x^*)\right)dx^* \tag{10}$$

where $\tilde{C}_{p\alpha 0}(x^*)$ and $\tilde{C}_{ph0}(x^*)$ are the magnitudes of the unsteady pressure fluctuation for torsion and heaving, respectively; $\psi_\alpha$ and $\psi_h$ are the phase differences for torsion and heaving, respectively; and $H_i^*$, $A_i^*$ ($i$=1, 2, 3, 4) are the flutter derivatives.

Under the action of self-excited lift and pitching moment, the flutter equations of a bridge surrounded by the smooth flow are expressed as follows

$$m\left(\ddot{h} + 2\xi_h\omega_h\dot{h} + \omega_h^2 h\right) = \frac{1}{2}\rho U^2(2B)\left\{KH_1^*\frac{\dot{h}}{U} + KH_2^*\frac{B\dot{\alpha}}{U} + K^2H_3^*\alpha + K^2H_4^*\frac{h}{B}\right\} \tag{11}$$

$$I(\ddot{\alpha} + 2\xi_\alpha\omega_\alpha\dot{\alpha} + \omega_\alpha^2\alpha) = \frac{1}{2}\rho U^2(2B^2)\left\{KA_1^*\frac{\dot{h}}{U} + KA_2^*\frac{B\dot{\alpha}}{U} + K^2A_3^*\alpha + K^2A_4^*\frac{h}{B}\right\} \tag{12}$$

where $m$ and $I$ are the mass and the mass moment of inertia respectively; $\xi_h$ and $\xi_\alpha$ are the vertical and torsional damping ratios respectively; $\omega_h$ and $\omega_\alpha$ are the structural natural frequencies in vertical and torsional directions, respectively; $K$ (=$\omega B/U$, $\omega$ the circular frequency of vibration, $B$ the width of bridge) is the reduced frequency; $h$ and $\alpha$ are the vertical and torsional displacements of bridge, respectively; and the dot on the cap denotes the derivative with respect to the time.

The flutter derivatives of the plate with different slot ratios under 0°, 2°, 4°, 6°, 8° and 10° angles of attack are calculated. The direct flutter derivatives, $H_1^*$ and $A_2^*$, and the coupled flutter derivatives, $H_3^*$ and $A_1^*$, are shown in Figs. 11-14, respectively.

At 0° and 2° angles of attack, as the values of $H_1^*$ and $A_2^*$ are always negative, the uncoupled self-excited forces provide positive damping and result in an increase in the system damping which is favorable to the stability of vertical and torsional motions. The negative damping generated by the coupled forces, the aerodynamic stiffness terms $H_3^*$ and $A_1^*$ in particular, is the main contributing source that drives the bridge to coupled flutter instability observed by Chen and Kareem (2006). With the increase in slot ratio, the absolute values of $H_3^*$ and $A_1^*$ both decrease which is favorable to the flutter stability.

At larger angles of attack, the variations of $H_1^*$, $A_1^*$ and $A_2^*$ of the plate without slot versus reduced wind velocity will change, and this phenomenon is intensified by the existence of central slot. With the increase in angle of attack and slot ratio, the direct flutter derivatives, $A_2^*$ and $H_1^*$, change their signs from negative to positive successively, which implies the torsional flutter and the single-vertical-mode flutter, i.e., galloping, may be developed.

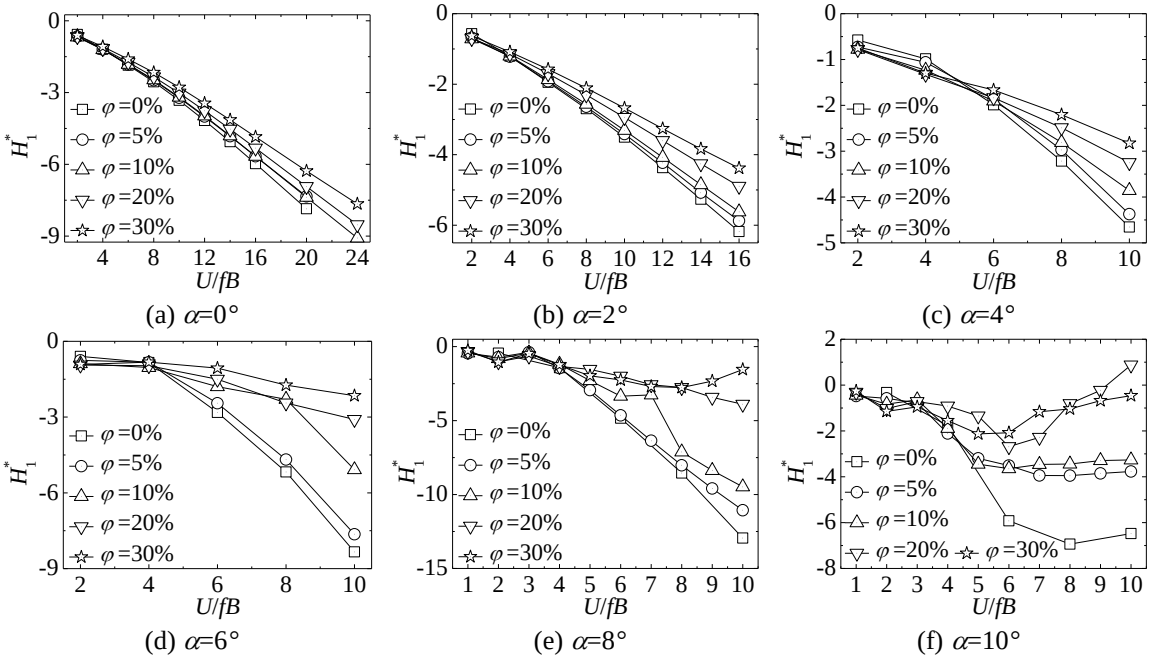


Fig. 11 Flutter derivatives of central-slotted plate ($H_1^*$)

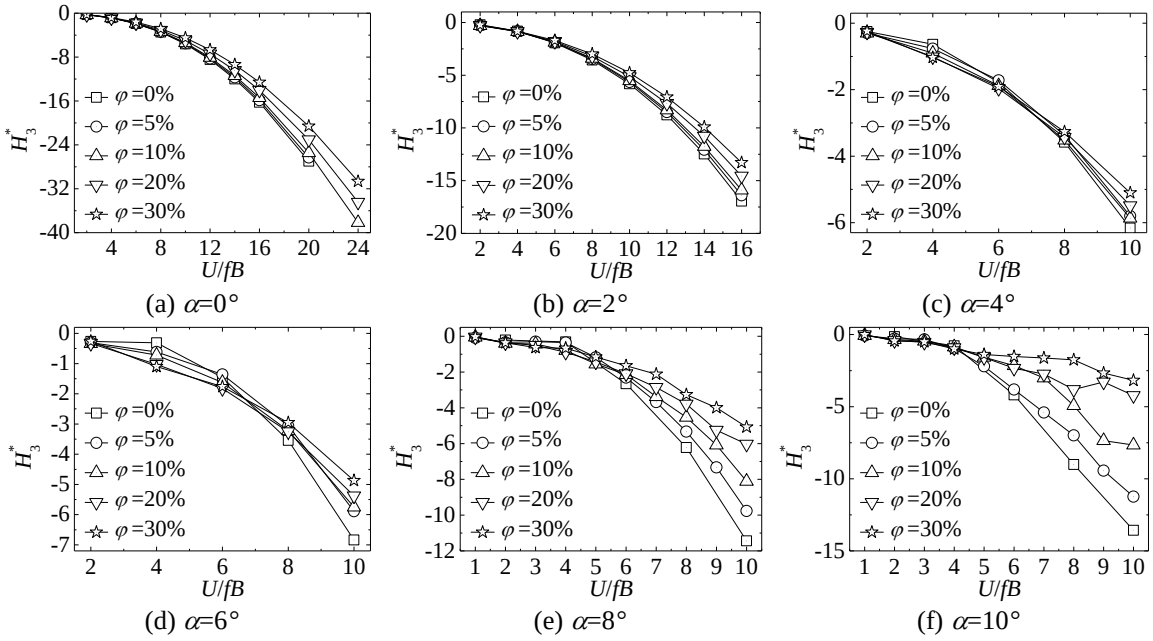


Fig. 12 Flutter derivatives of central-slotted plate ($H_3^*$)

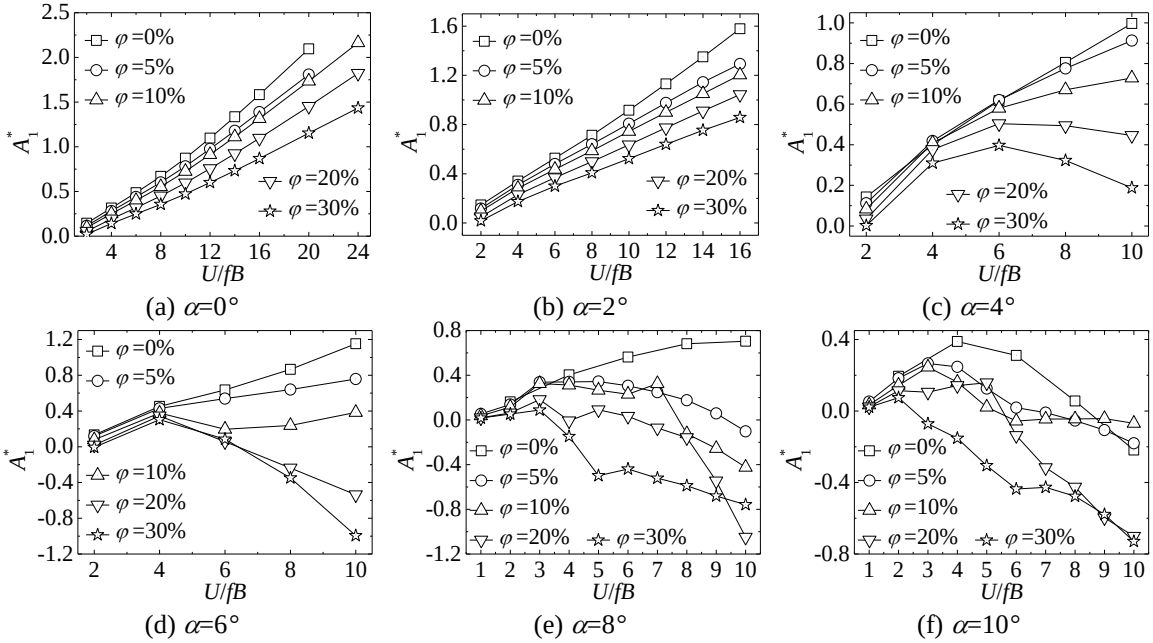


Fig. 13 Flutter derivatives of central-slotted plate ($A_1^*$)

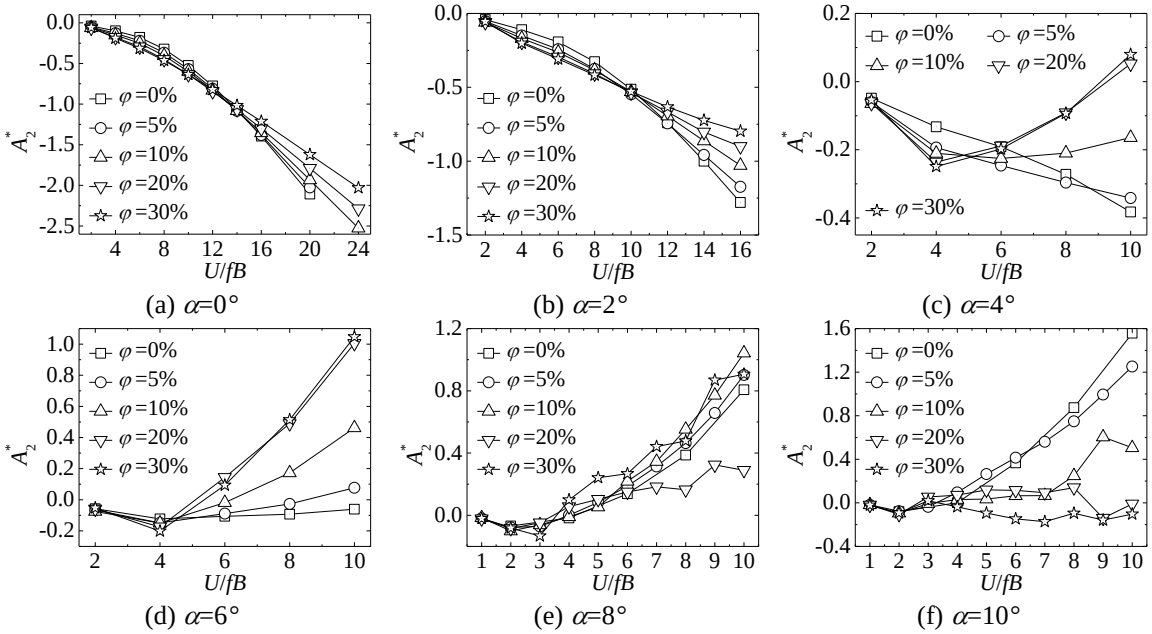


Fig. 14 Flutter derivatives of central-slotted plate ($A_2^*$)

## 3. Flutter performance of a long-span suspension bridge

A realistic suspension bridge located in mountainous canyon area with center span of 1100 m is used as an example. The two main cable planes are 27 m apart and the bridge deck is suspended by hangers at intervals of 10 m. The mass and the mass moment of inertia are $3.29\times10^4$ kg and $3.32\times10^6$ kg·m per meter respectively. The finite element model of the suspension bridge is established using ANSYS software, and some natural frequencies of modes are shown in Table 2.

Then, the self-excited forces on the main girder are considered to analyze the flutter performance of the suspension bridge of which the flutter derivatives are calculated from the plate. Based on the Scanlan's linearized model, many analysis methods for flutter in the frequency domain have been developed, including Chen *et al.* (2000), Ge and Tanaka (2000), Ding *et al.* (2002), Hua *et al.* (2007). In this paper, a three-dimensional full-order analysis method using ANSYS software is applied to analyze the flutter performance of the bridge. The aeroelastic stiffness matrices and damping matrices are represented by a pair of Matrix27 elements which are attached to each node in the element of girder. If the system has n DOFs, there will be *n* conjugate pairs of complex eigenvalues and eigenvectors. The *j*th conjugate pair of complex eigenvalues can be expressed as $\lambda_j = -\xi_j\omega_j \pm \omega_j\sqrt{1-\xi_j^2}$ ($j$=1, 2, …, n), where $\xi_j$ and $\omega_j$ are *j*th modal damping and frequency, respectively. The system is dynamically unstable if one of the modal damping is negative beyond the critical flutter wind velocity.

Firstly, the effects of angle of attack on flutter performance of the bridge are analyzed. In addition to the computed flutter derivatives of the plate without slot, the flutter derivatives based on the Theodorsen function are also used for comparison. The predicted critical flutter wind speed and flutter frequency are summarized in Table 3.

Table 2 Modal frequencies and shapes of the suspension bridge

| Order number | 1 | 4 | 5 | 10 | 13 |
|---|---|---|---|---|---|
| Frequency (Hz) | 0.054 | 0.153 | 0.218 | 0.289 | 0.325 |
| Vibration mode | Symmetric lateral bending - Girder | Symmetric vertical bending - Girder | | Swing - Cable | Symmetric Torsional - Girder |

Table 3 Flutter conditions of the bridge with plate deck

| Angle of attack | Branch | Velocity (m/s) | Frequency (Hz) |
|---|---|---|---|
| Based on Theodorsen function | | | |
| 0° | mode 10 | 89.8 | 0.262 |
| Based on computed flutter derivatives | | | |
| 0° | mode 10 | 90.5 | 0.258 |
| 2° | mode 10 | 86.7 | 0.258 |
| 4° | mode 10 | 72.0 | 0.273 |
| 6° | mode 10 | 50.9 | 0.286 |
| 8° | mode 13 | 35.0 | 0.314 |
| 10° | mode 13 | 31.2 | 0.316 |

Figs. 15 and 16 show the changes in the real and imaginary parts of complex eigenvalues as the wind velocity is increased. The flutter conditions calculated by the computed flutter derivatives agree with that by Theodorsen function at 0° angle of attack. The angle of attack is a negative factor for the flutter performance of the bridge, and the critical flutter wind speed decreases with the increase in angle of attack. At lower angles of attack, the plate presents the characteristic of streamlined body. As heaving and torsional motions have strong coupling effect at the flutter critical state, the flutter frequency is between the first symmetrical vertical bending frequency (0.153 Hz) and the first symmetrical torsional frequency (0.325 Hz). It seems that the flutter critical state is determined by the complex mode 10 corresponding to the swing mode of main cable. Actually, the properties of the complex mode 10 and the complex mode 13 corresponding to the first symmetric torsional mode have been switched at a certain wind velocity when their frequencies become close, referred to curve-veering phenomena (Chen and Kareem 2003). The symmetric vertical bending and torsional modes, i.e., modes 4 and 13, are most important modes for this coupled flutter. The flutter critical state of the bridge is determined by the complex mode 13 when the angle of attack increases to 8° or 10°, and the flutter frequency is very close to the first symmetrical torsional frequency, which means the coupled bending-torsional flutter of bridge gradually converts to the torsional flutter.

Then, the effects of central slot on flutter performance of the bridge are analyzed based on the computed flutter derivatives of central slotted plates. The predicted flutter conditions are summarized in Table 4, and Fig. 17 shows the changes in modal damping of flutter modal branch as the wind velocity is increased. The existence of central slot has different effects on flutter performance of the bridge at different angles of attack. For 0°and 2° angles of attack, with the increase in slot ratio, the critical flutter wind speed increases, but the flutter frequency is unchanged.

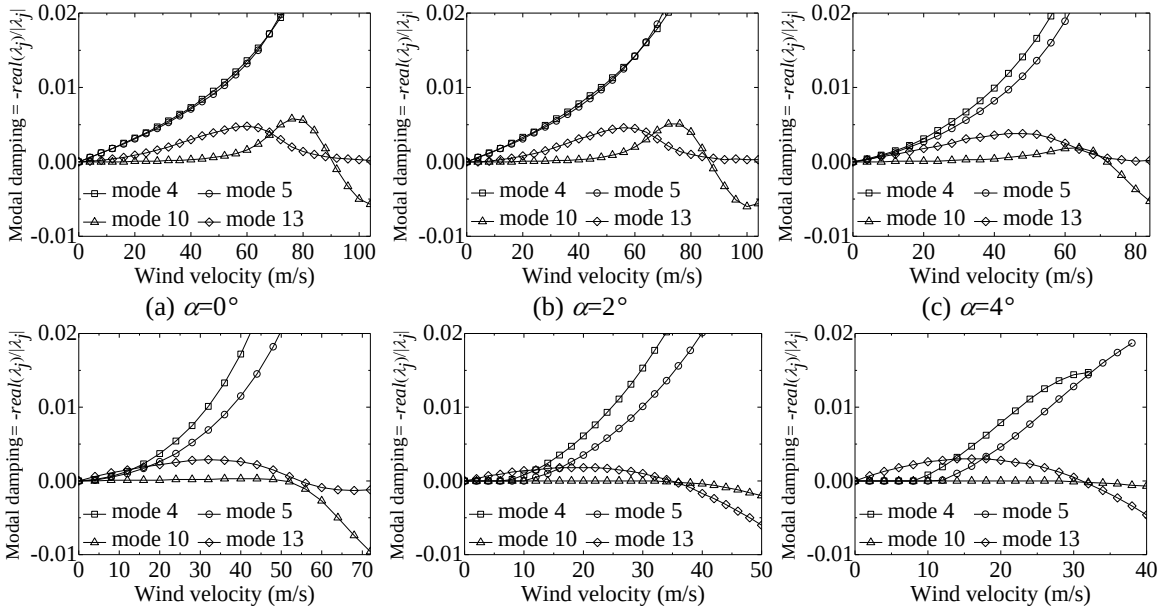


Fig. 15 Real part of complex eigenvalues versus wind velocity

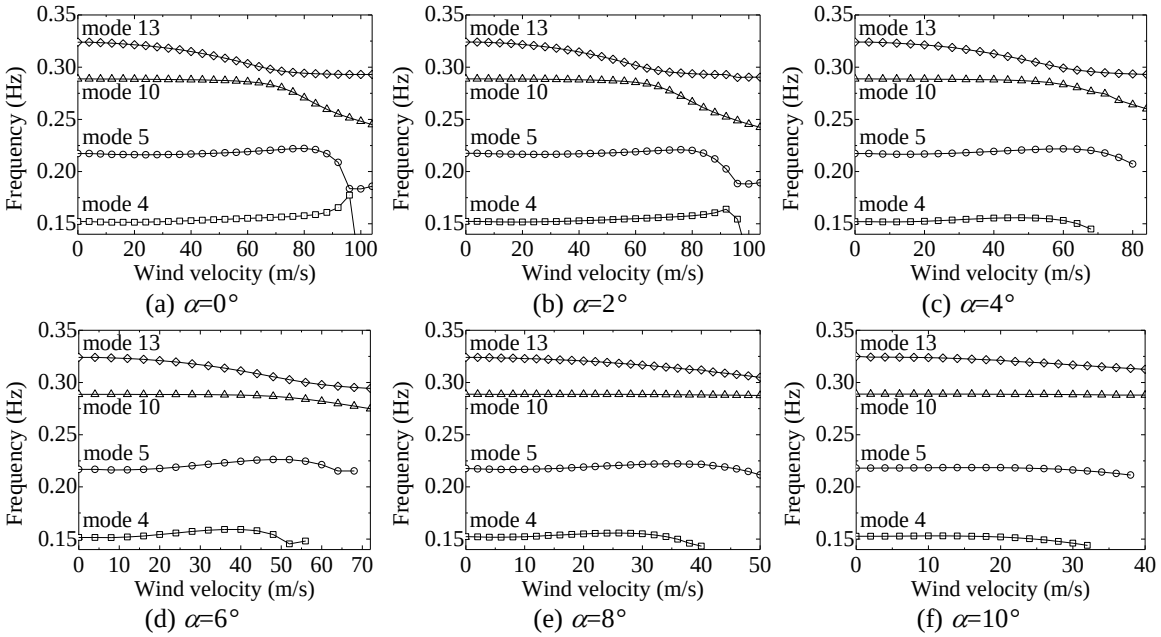


Fig. 16 Imaginary part of complex eigenvalues versus wind velocity

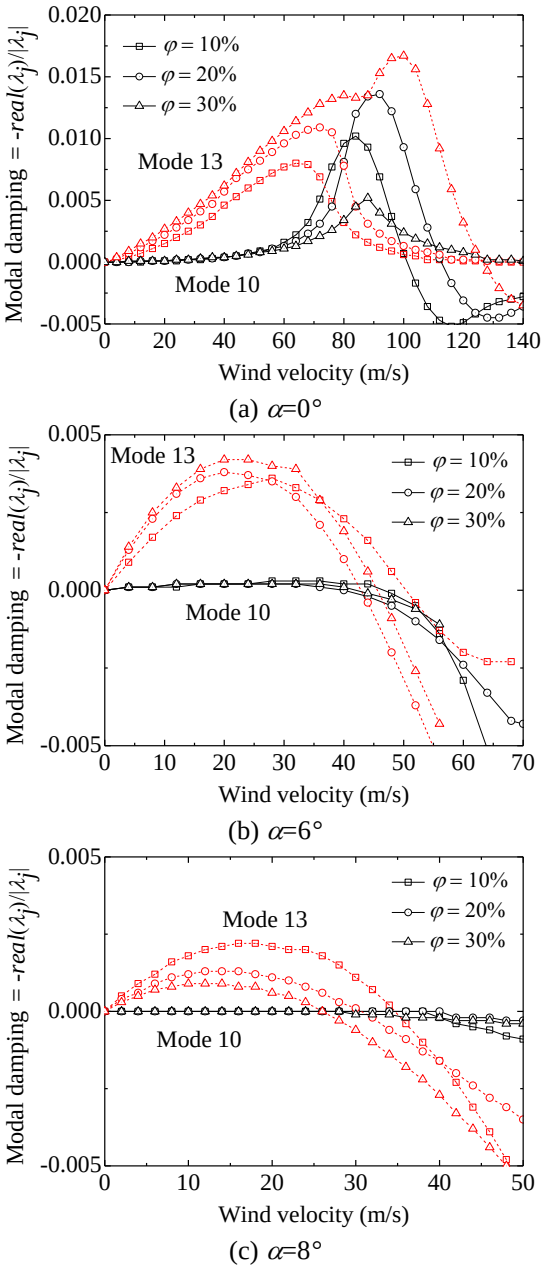


Fig. 17 Modal damping of flutter modal branch versus wind velocity

The central slot improves the absolute value of system damping of the complex mode corresponding to the first symmetric torsional mode, so the modal damping of this mode changes its sign from positive to negative at a higher wind speed. For $\varphi$=30% when the absolute value of system damping of the mode 13 is large enough, the properties of the complex modes 10 and 13 are not switched anymore, and the flutter critical state of the bridge is determined by the complex modal branch 13.

Table 4 Flutter conditions of the bridge with central-slotted plate deck

| Angle of attack | $\varphi$= 5% | $\varphi$= 10% | $\varphi$= 15% | $\varphi$= 20% | $\varphi$= 30% |
|---|---|---|---|---|---|
| Velocity (m/s) | | | | | |
| 0° | 96.9 | 101.2 | 106.3 | 112.6 | 126.3 |
| 2° | 93.5 | 95.7 | 100.0 | 103.4 | 110.8 |
| 4° | 75.6 | 70.8 | 66.5 | 64.7 | 65.0 |
| 6° | 51.0 | 47.0 | 43.3 | 42.8 | 45.7 |
| 8° | 33.0 | 34.7 | 30.0 | 30.5 | 26.0 |
| 10° | 25.3 | 22.0 | 29.0 | 31.0 | 23.0 |
| Frequency (Hz) | | | | | |
| 0° | 0.253 | 0.253 | 0.253 | 0.252 | 0.250 |
| 2° | 0.252 | 0.255 | 0.254 | 0.254 | 0.256 |
| 4° | 0.271 | 0.278 | 0.282 | 0.284 | 0.286 |
| 6° | 0.286 | 0.286 | 0.311 | 0.312 | 0.312 |
| 8° | 0.316 | 0.317 | 0.318 | 0.320 | 0.322 |
| 10° | 0.319 | 0.321 | 0.321 | 0.322 | 0.324 |

For 4° and 6° angles of attack, with the increase in slot ratio, the flutter frequency increases and the critical flutter wind speed shows a decreasing tendency. The effects of the slot ratio and the angle of attack on flutter performance of the bridge are very similar. Although the absolute value of system damping of the complex mode 13 can be improved by central slot at lower wind speeds, its sign changes from negative to positive in advance. For 8° and 10° angles of attack, the flutter frequencies are all close to the first symmetrical torsional frequency, and the central slot is still a negative factor for the flutter performance of the bridge. The absolute value of system damping of the complex mode 13 decreases with the increase in slot ratio and becomes zero in advance. After the flutter critical state, the damping ratio of the mode 4 corresponding to the first symmetric vertical mode also changes its sign from positive to negative with the further increase in wind speed.

In summary, the central slot can improve the critical flutter wind speed of plate at lower angles of attack, but it becomes a negative factor when the angle of attack is large enough to make a streamlined plate present the characteristics of bluff body.

## 4. Conclusions

In this study, the effects of central slot at large angles of attack on flutter performance of a suspension bridge with plate deck are analyzed and the following conclusions are made:

(1) The angle of attack is a negative factor for the flutter performance of the bridge, and the critical flutter wind speed decreases with the increase in angle of attack. The streamlined plate presents the characteristics of bluff body at larger angles of attack, and the size of the vortex formed on the leading edge and its movement distance along the plate increase, which means the coupled bending-torsional flutter of bridge gradually converts to the torsional flutter.

(2) When the angle of attack is small, including 0° and 2°, the existence of central slot can improve the flutter performance of the bridge. The streamlined characteristics of the plate are not changed by the existence of central slot due to the weak aerodynamic interference between

the upstream and downstream plates. With the increase in slot ratio, the absolute values of the aerodynamic stiffness terms, $H_3^*$ and $A_1^*$, both decrease, and the critical flutter wind speed increases but the flutter frequency keeps the same value which is between the first symmetrical vertical bending and the first symmetrical torsional frequencies.

(3) When the angle of attack is large, including 4°, 6°, 8° and 10°, the central slot becomes a negative factor for the flutter performance of the bridge. The central slot makes the plate further present the characteristics of bluff body, and the vortex shedding is even excited when the slot ratio increases to a critical value. With the increase in slot ratio, the direct flutter derivative, $A_2^*$, changes its sign from negative to positive in advance, so the flutter frequency is gradually close to the first symmetrical torsional frequency and the critical flutter wind speed shows a decreasing tendency. As the accuracy of CFD simulations for vibrating plate at large angles of attack is not confirmed, these results are yet to be proved by further wind tunnel tests.

## Acknowledgments

The authors are grateful for the financial supports from the National Natural Science Foundation of China (51525804), the Construction Technology Project of China Transport Ministry (2014318800240) and the Sichuan Province Youth Science and Technology Innovation Team (2015TD0004).

## References

Amandolese, X., Michelin, S. and Choquel, M. (2013), "Low speed flutter and limit cycle oscillations of a two-degree-of-freedom flat plate in a wind tunnel", *J. Fluid. Struct.*, **43**, 244-255.

Chen, X.Z. and Kareem, A. (2003), "Curve veering of eigenvalue loci of bridges with aeroelastic effects", *J. Eng. Mech. - ASCE*, **129**(2), 146-159.

Chen, X.Z. and Kareem, A. (2006), "Revisiting multimode coupled bridge flutter: some new insights", *J. Eng. Mech. - ASCE*, **132**(10), 1115-1123.

Chen, X.Z., Matsumoto, M. and Kareem, A. (2000), "Aerodynamic coupled effects on flutter and buffeting of bridges", *J. Eng. Mech. - ASCE*, **126**(1), 17-26.

Diana, G., Resta, F., Belloli, M. and Rocchi, D. (2006), "On the vortex shedding forcing on suspension bridge deck", *J. Wind Eng. Ind. Aerod.*, **94**, 341-363.

Ding, Q.S., Chen, A.R. and Xiang, H.F. (2002), "Coupled flutter analysis of long-span bridges by multimode and full-order approached", *J. Wind Eng. Ind. Aerod.*, **90**(12-15), 1981-1993.

Ge, Y.J. and Tanaka, H. (2000), "Aerodynamic flutter analysis of cable-supported bridges by multi-mode and full-mode approaches", *J. Wind Eng. Ind. Aerod.*, **86**(2-3), 123-153.

Hua, X.G., Chen, Z.Q., Ni, Y.Q. and Ko, J.M. (2007), "Flutter analysis of long-span bridges using ANSYS", *Wind Struct.*, **10**(1), 61-82.

Huang, L., Liao, H. L., Wang, B. and Li, Y. L. (2009), "Numerical simulation for aerodynamic derivatives of bridge deck", *Simul. Model. Pract. Th.*, **17**, 719-729.

Kwok, K.C.S., Qin, X.R., Fok, C.H. and Hichcock, P.A. (2012), "Wind-induced pressures around a sectional twin-deck bridge model: effects of gap-width on the aerodynamic forces and vortex shedding mechanisms", *J. Wind Eng. Ind. Aerod.*, **110**, 50-61.

Lee, S., Kwon, S.D. and Yoon, J. (2014), "Reynolds number sensitivity to aerodynamic forces of twin box bridge girder", *J. Wind Eng. Ind. Aerod.*, **127**, 59-68.

Matsumoto, M. (1996), "Aerodynamic damping of prisms", *J. Wind Eng. Ind. Aerod.*, **59**, 159-175.
Miranda, S., Patruno, L., Ricci, M. and Ubertini, F. (2015), "Numerical study of a twin box bridge deck with increasing gap ratio by using RANS and LES approaches", *Eng. Struct.*, **99**, 546-558.
Sato, H., Hirahara, N., Fumoto, K., Hirano, S. and Kusuhara, S. (2002), "Full aeroelastic model test of a super long-span bridge with slotted box girder", *J. Wind Eng. Ind. Aerod.*, **90**(12-15), 2023-2032.
Sato, H., Kusuhara, S., Ogi, K. and Matsufuji, H. (2000), "Aerodynamic characteristics of super long-span bridges with slotted box girder", *J. Wind Eng. Ind. Aerod.*, **88**, 297-306.
Trein, C.A., Shirato, H. and Matsumoto, M. (2015), "On the effects of the gap on the unsteady pressure characteristics of two-box bridge girders", *Eng. Struct.*, **82**, 121-133.
Yang, Y.X., Wu, T., Ge, Y.J. and Kareem, A. (2015), "Aerodynamic stabilization mechanism of a twin box girder with various slot widths", *J. Bridge Eng.*, **20**(3).
Yang, Y.X., Zhou, R., Ge, Y.J., Mohotti, D. and Mendis, P. (2015), "Aerodynamic instability performance of twin box girders for long-span bridges", *J. Wind Eng. Ind. Aerod.*, **145**, 196-208.
Zhang, Z.T., Ge, Y.J. and Yang, Y.X. (2013), "Torsional stiffness degradation and aerostatic divergence of suspension bridge decks", *J. Fluid. Struct.*, **40**, 269-283.
Zhu, Q. and Xu, Y.L. (2014), "Characteristics of distributed aerodynamic forces on a twin-box bridge deck", *J. Wind Eng. Ind. Aerod.*, **131**, 31-45.

*AD*